Chemical Science

ROYAL SOCIETY OF CHEMISTRY

EDGE ARTICLE

View Article Online
View Journal | View Issue

Cite this: *Chem. Sci.*, 2024, **15**, 7586

All publication charges for this article have been paid for by the Royal Society of Chemistry

Received 28th January 2024
Accepted 14th April 2024

DOI: 10.1039/d4sc00656a

rsc.li/chemical-science

Crystalline nanosheets of three-dimensional supramolecular frameworks with uniform thickness and high stability†

Xinxin Wang, Yucheng Jin, Tianyu Zheng, Ning Li, Yuesheng Han, Baoqiu Yu, Kang Wang,* Dongdong Qi,* Tianyu Wang* and Jianzhuang Jiang*

Fabricating three dimensional (3D) supramolecular frameworks (SMFs) into stable crystalline nanosheets remains a great challenge due to the homogeneous and weak inter-building block interactions along 3D directions. Herein, crystalline nanosheets of a 3D SMF with a uniform thickness of 4.8 ± 0.1 nm immobilized with Pt nanocrystals on the surface (Q[8]/Pt NSs) were fabricated *via* the solid–liquid reaction between cucurbit[8]uril/H_2PtCl_6 single crystals and hydrazine hydrate with the help of gas and heat yielded during the reaction process. A series of experiments and theoretical calculations reveal the ultrahigh stability of Q[8]/Pt NSs due to the high density hydrogen bonding interaction among neighboring Q[8] molecules. This in turn endows Q[8]/Pt NSs with excellent photocatalytic and continuous thermocatalytic CO oxidation performance, representing the thus-far reported best Pt nanomaterial-based catalysts.

Introduction

Organic molecule-based frameworks including supramolecular frameworks (SMFs),[1,2] metal–organic frameworks (MOFs),[3,4] and covalent organic frameworks (COFs)[5–8] have exhibited great application potentials in various areas such as gas storage and separation,[9–15] catalysis,[16–20] sensing,[21–24] enzyme encapsulation,[25,26] and proton conduction[27,28] due to their periodic porous structure and functional diversity. Crystalline materials with ultrathin nanosheet morphology have aroused significant research interest in the past two decades since the report of graphene in 2004.[29] Towards further tailored structures, pores, and functionalities, a wide range of two dimensional (2D) bulk SMFs,[30,31] MOFs,[4,32,33] and COFs[34–39] composed of layered nanostructural components have been easily fabricated into ultrathin crystalline nanosheets depending on the heterogeneous inter-building block interactions, by means of either top-down or bottom-up methods on the basis of the commonly employed strategy through intensifying the intra-layer inter-building block interactions and simultaneously weakening the inter-layer supramolecular interactions. This, however, is not the case for the three dimensional (3D) analogous frameworks due to the homogeneous inter-building block interactions along the 3D directions. Among the 3D organic molecule-based frameworks, 3D MOFs were firstly fabricated into stable crystalline nanosheets by top-down and bottom-up methods in 2016 (ref. 40) and 2018,[41] respectively, because of their moderate inter-building block coordination bonding interaction intensity, which is "weak" enough to be broken down but "strong" enough to maintain the fragile continuous networks with few-nanometer thickness.[41–43] In 2021, crystalline 3D COF thin films were also successfully fabricated by a bottom-up solid–liquid/liquid–liquid interfacial synthesis approach depending on selectively confining the crystal growth of 3D COFs.[44–47] However, pure supramolecular interactions including the hydrogen bond, π–π interaction, and van der Waals force interactions are conventionally considered too weak to support the fabrication and isolation of stable nanosheets of 3D SMFs due to the homogeneous and weak inter-building block interactions. Obviously, realizing the stable crystalline nanosheets for 3D SMFs will significantly expand the range of ultrathin crystalline molecule-based framework materials with enlarged surface and structural features for enhanced functionalities and diverse application potentials.

Herein, we describe the fabrication of crystalline nanosheets of a 3D cucurbit[8]uril (Q[8]) SMF *via* direct chemical synthesis. A solid–liquid reaction between the Q[8]/H_2PtCl_6 single crystals dispersed in water and liquid hydrazine hydrate affords ultrathin supramolecular nanosheets of Q[8] decorated with platinum particles (Q[8]/Pt NSs) with a uniform thickness of 4.8 ± 0.1 nm and ultrastability, according to the transmission electron microscopy (TEM) and atomic force microscopy (AFM)

Beijing Advanced Innovation Center for Materials Genome Engineering, Beijing Key Laboratory for Science and Application of Functional Molecular and Crystalline Materials, Department of Chemistry and Chemical Engineering, School of Chemistry and Biological Engineering, University of Science and Technology Beijing, Beijing 100083, China. E-mail: kangwang@ustb.edu.cn; qdd@ustb.edu.cn; twang@ustb.edu.cn; jianzhuang@ustb.edu.cn

† Electronic supplementary information (ESI) available. See DOI: https://doi.org/10.1039/d4sc00656a

images. Powder X-ray diffraction (PXRD) analysis discloses the crystalline nature of the Q[8] nanosheets and Pt nanocrystals. Experimental investigations in combination with theoretical calculations reveal the important role of explosive gases (N_2 and HCl) and heat yielded during the chemical reaction process in the formation of the nanosheets of 3D SMF and the high density hydrogen bonding interaction in stabilizing the Q[8]/Pt NSs. A series of spectroscopic technologies including Fourier transform infrared (FT-IR), X-ray absorption structure (XAS), and X-ray photoelectron spectroscopy (XPS) unveil the immobilization of Pt nanocrystals onto the surface of Q[8] nanosheets through O–Pt coordinating interactions, endowing the immobilized Pt nanocrystals with significantly enhanced stability. This in turn results in an excellent photocatalytic and, in particular, continuous thermocatalytic CO oxidation performance of Q[8]/Pt NSs with high CO-to-CO_2 conversion efficiency and good durability, representing the thus-far reported best Pt nano-material-based catalysts.

Results and discussion

Q[8] represents a well-known cucurbit[*n*]uril compound with a typical 3D SMF structure. Fig. 1 depicts its single crystal structure on the basis of CCDC-1052403. As can be seen, in the Q[8] single crystal, each Q[8] molecule (the central Q[8]) is fixed by four neighbouring Q[8] molecules with 16 bifurcated $(C–H)_2\cdots O{=}C$ hydrogen bonds. The portal carbonyls of the central Q[8] are close to the outer surface of two neighbouring Q[8] molecules, while the outer surface of the central Q[8] is close to the portal carbonyls of the other two neighbouring Q[8] molecules. This reciprocal interaction leads to a quasi-T_d symmetry for the unit formed by the five Q[8] molecules, which further extends into a 3D hydrogen-bonded network, Fig. 1. It is worth noting that the multiple hydrogen-bonding interactions existing between neighbouring Q[8] molecules endow this Q[8] SMF with comparable stability to 3D MOFs and 3D COFs, as proved by its unchanged crystal structure after immersing the Q[8] single crystal into various organic solvents (*e.g.*, DMF and DMSO), boiling water, H_2O_2, strong acid (6.0 M HCl), and strong base (10.0 M NaOH) for 24 h, Fig. S1.† Such strong and homogeneous inter-building block interactions, however, also result in the failure in exfoliating the Q[8] single crystal into nanosheets *via* conventional strategies including sonication and mechanical delamination, Fig. S2.† Herein, the reaction between the block-shaped Q[8]/H_2PtCl_6 single crystals with a similar arrangement of Q[8] molecules dispersed in water with liquid $N_2H_4\cdot H_2O$ at 50 °C for 1 hour yields ordered square nanosheets, Q[8]/Pt NSs, as indicated by the SEM images, Fig. 2a, S3 and S4.† In addition, the reaction time and concentration of $N_2H_4\cdot H_2O$ have been varied to optimize the fabrication process of Q[8]/Pt NSs, Fig. S5–S7.† In the case of Q[8]/Pt NSs, the nanosheets appear after reaction for 10 minutes at 50 °C. Along with further increase in the reaction time, the amount of nanosheets increases, accompanied by the gradual disappearance of the block-shaped crystals of Q[8]/H_2PtCl_6. After reaction for 1 hour, only nanosheets can be observed from TEM and SEM images, revealing the complete conversion of Q[8]/H_2PtCl_6 to Q[8]/Pt NSs. Moreover, the nanosheets gradually become thinner with the increase in the $N_2H_4\cdot H_2O$ concentration to 12 mmol L^{-1}, Fig. S7.† Further increase in the $N_2H_4\cdot H_2O$ concentration leads to the decrease in the amount of nanosheets accompanied by the gradual increase in the block-shaped crystals of Q[8]/Pt. As a result, Q[8]/Pt NSs prepared from Q[8]/H_2PtCl_6 with 12 mmol per L $N_2H_4\cdot H_2O$ at 50 °C for 1 hour were therefore used for the detailed investigation in the present work. In particular, the optimized fabrication process of Q[8]/Pt NSs has been carried out for three times, giving almost the same PXRD patterns and almost the same morphology as revealed by the TEM and SEM images, Fig. S8 and S9,† demonstrating the excellent reproducibility of the preparation method. Moreover, the large-scale preparation of Q[8]/Pt NSs can be easily achieved by using the present method, Fig. S10,† fulfilling the requirement for large-scale production. AFM measurements prove the smooth surface of Q[8]/Pt NSs with a uniform thickness of *ca.* 4.8 ± 0.1 nm, corresponding to the thickness of six Q[8] layers along the *b* direction in the Q[8] single crystal, Fig. 2b and c. TEM image reveals the transparent square-like morphology of Q[8]/Pt NSs with the edge length of several micrometers, Fig. 3a, confirming their ultrathin nanosheet nature. Further evidence for this point comes from the clear observation of the Tyndall effect when a red laser is passed through the dispersed ethanol solution of Q[8]/Pt NSs, inset in Fig. 3a. The highly ordered periodic structure of Q[8]/Pt NSs was characterized by high-resolution TEM (HR-TEM) and fast

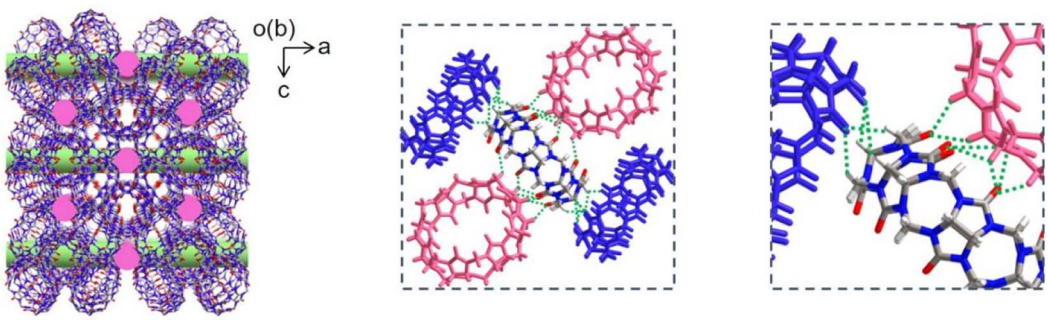

Fig. 1 Crystal stacking structure in the Q[8] crystal from the *ac* plane (left) and detailed interactions between the central Q[8] molecule and four neighboring Q[8] molecules in the Q[8] crystal (middle and right) on the basis of CCDC-1052403.

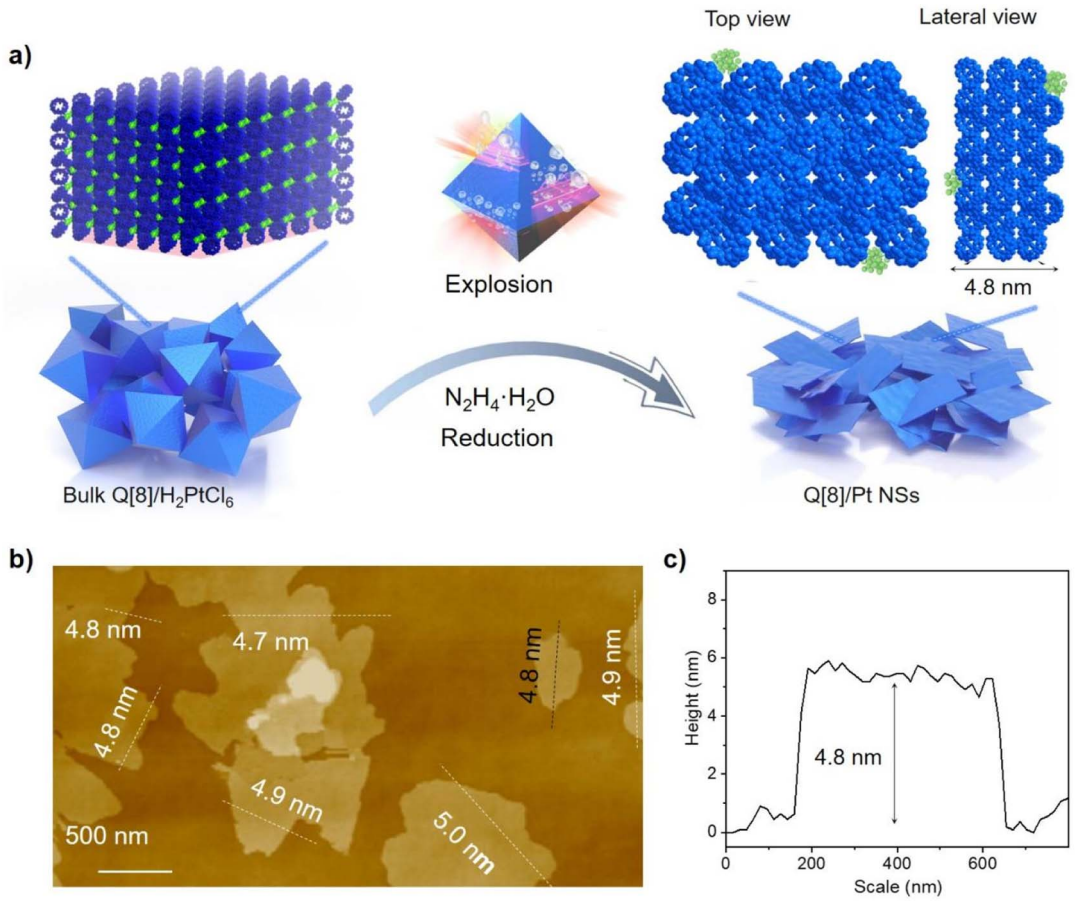

Fig. 2 Fabricating the crystalline ultrathin Q[8]/Pt NSs from the bulk Q[8]/H_2PtCl_6 single crystal. (a) Schematic illustration of the formation of Q[8]/Pt NSs *via* the solid–liquid reaction between Q[8]/H_2PtCl_6 single crystals and an aqueous solution of $N_2H_4 \cdot H_2O$ with the help of a large amount of gas and heat yielded during the chemical reaction process. (b) The AFM image and (c) corresponding height profile of Q[8]/Pt NSs after sonication in ethanol for 5 min.

Fourier transform (FFT) images, Fig. 3b and c. HR-TEM demonstrates a clear quadrilateral network structure with a pore size of *ca.* 0.38 nm, consistent with the calculated channel cavity size of *ca.* 0.37–0.41 nm (*ca.* 0.22–0.26 nm after deducting the van der Waals radii of the atoms on the channel surface) for Q[8]/Pt NSs along the *b* axis on the basis of the single crystal structure of Q[8], Fig. S11 and S12.† Moreover, the Q[8] units can be identified as bright spots in the HR-TEM image, while the channel of Q[8]/Pt NSs is identified as slightly darker spots. The rectangle-shaped dark areas adjacent to the bright spots and the dimmer spots correspond to the curved channel in the Q[8]/Pt NSs, Fig. 3d and e, revealing the same arrangement of Q[8] molecules in the nanosheets with that in Q[8] single crystals. In particular, the selected area FFT image shows a highly ordered arrangement with independent diffraction points, confirming the high crystallinity of Q[8]/Pt NSs, inset in Fig. 3c. In addition, HR-TEM images unveil the widely dispersed Pt nanoparticles with a size of 2–10 nm on Q[8]/Pt NSs, revealing the reduction of H_2PtCl_6 into Pt^0, Fig. S13.† It is worth noting that the size of the Pt nanoparticles is significantly larger than the cavity size of the Q[8] molecule, indicating the location of Pt nanoparticles on the surface of Q[8]/Pt NSs. The pore size distribution of Q[8]/Pt NSs is calculated to be centred at *ca.* 0.3 nm on the basis of small-angle X-ray scattering (SAXS) analysis, consistent with the result according to the single crystal data of Q[8], Fig. S14.† Energy-dispersive X-ray spectroscopy (EDS) elemental mapping displays the homogeneous distribution of C and N atoms within Q[8]/Pt NSs, Fig. 3f. Inductively coupled plasma optical emission spectrometry analysis indicates 4.8% content of Pt in Q[8]/Pt NSs.

The crystalline structure of Q[8]/Pt NSs was further explored by PXRD. As shown in Fig. 3g and i, the PXRD pattern of Q[8]/Pt NSs displays a series of strong peaks at 8.1, 8.9, 9.2, 10.2, 12.0, 12.5, 13.5, 14.0, 15.3, 16.2, and 18.4°, which match well with the (211), (220), (112), (301), (321), (400), (411), (420), (303), (422), and (224) planes of the pattern of Q[8] single crystals, indicating the same arrangement of Q[8] molecules in the nanosheets as that in Q[8] single crystals, in line with the HR-TEM results. This is further confirmed by the Pawley refinement of the PXRD pattern with small agreement factors of $R_p = 4.24\%$ and $R_{wp} = 7.64\%$, Fig. S15.† Nevertheless, the PXRD pattern of Q[8]/Pt NSs also shows four peaks at 38.4, 44.0, 69.4, and 78.4°, corresponding to the (111), (200), (220), and (311) planes of hcp Pt

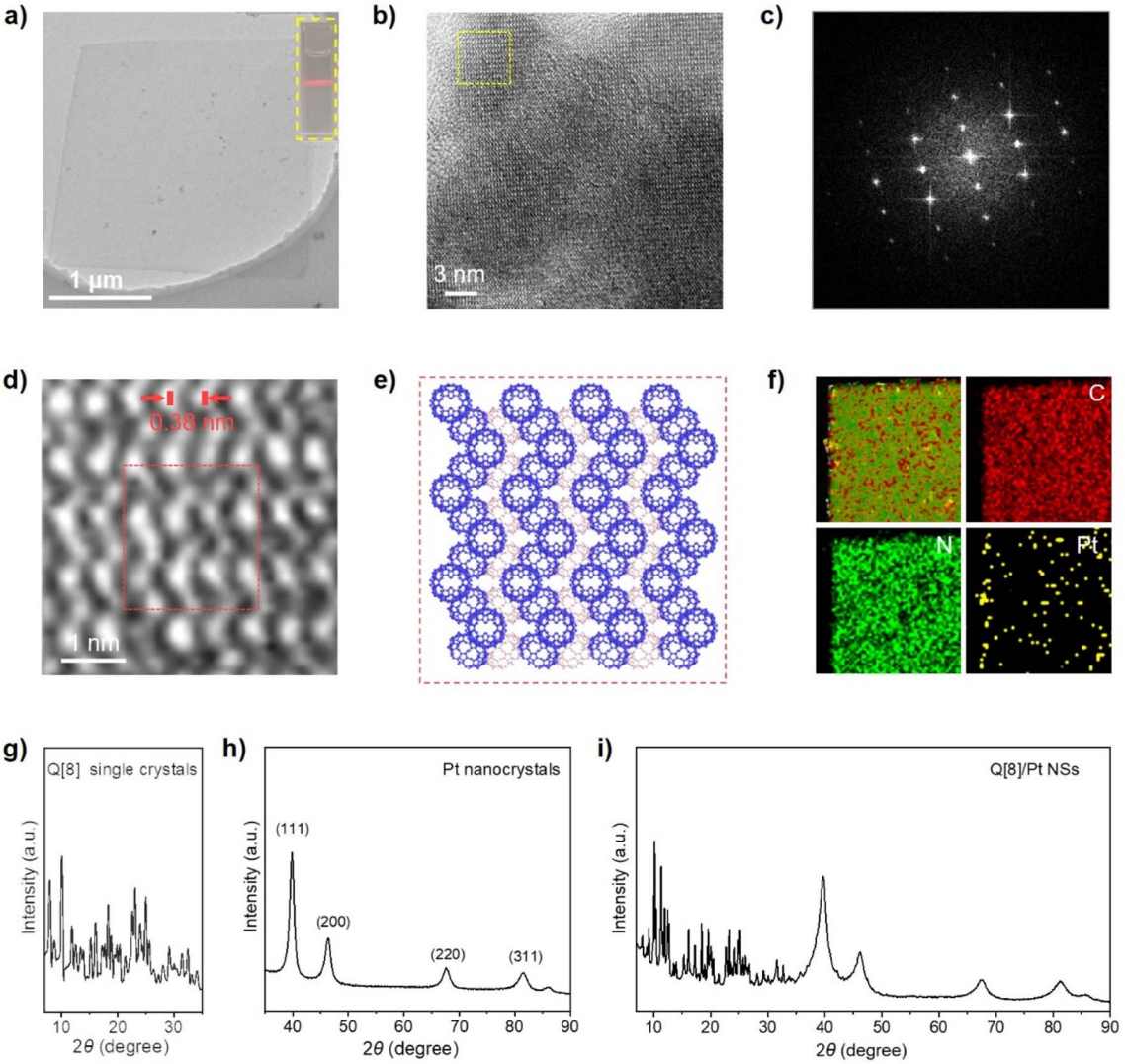

Fig. 3 Characterization of crystalline ultrathin Q[8]/Pt NSs. (a) TEM image of Q[8]/Pt NSs after sonication in ethanol for 5 min. Inset: the Tyndall effect of Q[8]/Pt NS dispersion in ethanol. (b) HRTEM image of Q[8]/Pt NSs after sonication in ethanol for 5 min. (c) Enlarged image of the area marked in (b) corresponding to the fast Fourier transform image and (d) enlarged HRTEM image of Q[8]/Pt NSs. (e) The curved channel in Q[8]/Pt NSs according to the X-ray crystal structure model of the *bc* plane. (f) EDS-elemental mapping images of Q[8]/Pt NSs. Experimental PXRD patterns of (g) Q[8] single crystals, (h) Pt nanocrystals, and (i) Q[8]/Pt NSs.

(PDF card no. 06-0663), disclosing the crystalline nature of the Pt nanoparticles, Fig. 3h and i. In addition, thermogravimetric analysis indicates that Q[8]/Pt NSs can be thermally stable up to 320 °C in air, Fig. S16.† Nevertheless, after being exposed to various organic solvents (*e.g.*, DMF and DMSO), boiling water, H_2O_2, strong acid (6.0 M HCl), and strong base (10.0 M NaOH) for 24 h, Q[8]/Pt NSs still exhibit unchanged PXRD patterns, Fig. S17,† demonstrating their excellent chemical stability owing to the multiple hydrogen-bonding interactions between neighbouring Q[8] molecules.

In the Pt 4f XPS spectrum, Q[8]/Pt NSs display two major peaks at 70.3 and 73.7 eV attributed to Pt^0 together with two weak peaks at 71.6 and 74.9 eV due to Pt^{2+},[48–50] Fig. S18.† The Pt^0/Pt^{2+} ratio amounts to 81 : 19 in Q[8]/Pt NSs, indicating the highly abundant zero-valence Pt in the nanocrystals. In the O 1s XPS spectrum of Q[8]/Pt NSs, in addition to a peak at 531.3 eV owing to C=O in Q[8],[50] a sign ascribed to C–O–Pt is also observed at 533.0 eV,[51] revealing the strong interaction between Pt nanocrystals and Q[8] in Q[8]/Pt NSs, Fig. S19.† Furthermore, a typical absorption peak due to the carbonyl band of Q[8] was observed at 1734 cm^{-1} in the FT-IR spectrum of pure Q[8], which shifts to 1724 cm^{-1} for Q[8]/Pt NSs, Fig. S20,† proving the effective bonding of Pt nanocrystals with the portal carbonyl groups of Q[8] in Q[8]/Pt NSs.[52] In addition, in the Pt L_3-edge X-ray absorption near-edge structure (XANES) spectrum, Fig. S21,† the energy position and spectral features of Q[8]/Pt NSs are similar to those for Pt foil, confirming the mainly zero valence metal state of Pt in Q[8]/Pt NSs. Moreover, the Pt L_3 extended X-ray absorption fine structure (EXAFS) spectrum in the *R* space of Q[8]/Pt NSs shows the peaks at 2.4 and 1.8 Å,

Fig. S22,† which are indexed as the Pt–Pt interaction and Pt–O coordination, respectively.[53–55] These results further demonstrate the domination of metallic Pt species and the existence of coordination interaction between Pt nanocrystals and Q[8] molecules in Q[8]/Pt NSs.

To understand the formation mechanism of the Q[8]/Pt NSs, both experimental and theoretical investigations have been carried out. According to eqn (1), drastic reduction of H_2PtCl_6 revealing the strong penetration not only produces the Q[8] crystalline layer in the same depth, but simultaneously yields a large amount of N_2 and HCl gases and releases a large amount of heat.

$$H_2PtCl_6 + N_2H_4{\cdot}H_2O \rightarrow Pt + N_2\uparrow + H_2O + 6HCl\uparrow,\quad \Delta_r H_m = -127\ \text{kJ mol}^{-1} \tag{1}$$

Combination of the gas-releasing explosive effect with the simultaneously yielding heat in turn leads to the successful exfoliation of the Q[8] crystalline nanosheets. This process proceeds in a repeated manner until the complete reduction of Q[8]/H_2PtCl_6 single crystals. Additional support for this point comes from the failed fabrication of the crystalline nanosheets starting from the same Q[8]/$H_2[PtCl_6]$ single crystals using weak reducing agents like methanol and glycol without yielding gas during the reduction reaction process, which however induces the isolation of Pt nanocrystal-immobilized Q[8] single crystals adopting the unchanged bulk morphology to the starting Q[8]/H_2PtCl_6 single crystals, Fig. S23–S26.† Actually, N_2 gas and heat release measurement result gives further support for the above-mentioned gas-releasing explosive effect. As shown in Fig. S27,† N_2 gas was detected as the sole gas product by GC spectroscopy and bright-field microscopy images since HCl yielded would dissolve in the aqueous reaction system once it leaves from the single crystals. In addition, as can be found, at the very beginning step of the reaction, the amount of N_2 gas increases in a gradual manner. However, after the reaction proceeds for 10 min, the amount of N_2 gas suddenly increases, suggesting the yielding process of the gas in a microscopic explosive manner at this time scale with a large amount of nanosheets formed, Fig. S28.† The temperature change in the reaction system was revealed by the thermal imager. As shown in Fig. S29,† the temperature increases from 50.1 to 52.6 °C after the reaction between 10.0 mg Q[8]/H_2PtCl_6 single crystals and 0.02 mL $N_2H_4{\cdot}H_2O$ for 10 min. On the basis of the above analysis, a two-step fabrication process for the nanosheets, Q[8]/Pt NSs, was proposed, Fig. S30 and S31:† (1) the reduction process from Pt^{IV} to Pt^0 together with the formation of Pt nanocrystals and (2) the formation of the crystalline ultrathin nanosheets of 3D SMF together with the formation of more Pt nanocrystals.

CO oxidation was selected as the probe reaction to investigate the catalytic performance of the Q[8]/Pt NSs due to the critical role of this reaction in cleaning air and fuel-cell applications.[55] Before the catalysis investigation, the free-standing flexible films of the Q[8]/Pt NSs, named Q[8]/Pt NS film-10/20/30/40, were fabricated through filtering 10/20/30/40 mg of Q[8]/Pt NS suspension in ethanol on the filter membrane, respectively, Fig. 4a and b. The cross-sectional SEM images of each membrane sample show a uniform thickness of 10, 20, 30, and 40 μm, respectively, Fig. 4c and S32.† For comparison, the film of 20 mg Q[8]/Pt material isolated from reducing Q[8]/H_2PtCl_6 using CH_3OH was also fabricated in the same manner, affording the CH_3OH-reduced Q[8]/Pt film-20.

The visible-light-driven photocatalytic CO oxidation performance of these films was investigated using an idealized gas mixture (0.8% CO, 20% O_2, and He balance) at 25 °C. GC spectroscopy was used to quantify the gaseous product. As shown in Fig. 4d and S33–S35,† CO could be oxidized to CO_2 under the photocatalysis of the Q[8]/Pt NS films with a CO_2 selectivity of 100%. The CO-to-CO_2 conversion rates of the Q[8]/Pt NS films with different thicknesses amount to 25.9, 28.3, 27.1, and 24.6 $mmol_{CO}\ g_{Pt}^{-1}\ h^{-1}$, respectively, Fig. 4e, corresponding to a turnover frequency (TOF) of 132, 145, 139, and 126 h^{-1}. In contrast, the CH_3OH-reduced Q[8]/Pt film-20 shows a CO conversion rate of 0.13 $mmol_{CO}\ g_{Pt}^{-1}\ h^{-1}$ with a TOF of 6.5 h^{-1}, Fig. S36,† much inferior to the Q[8]/Pt NS film-20. In particular, the result of the Q[8]/Pt NS films is superior to that of the commercial P25 TiO_2, and actually represents one of the best visible-light-driven photocatalytic CO oxidation performances in terms of catalytic efficiency, Table S1,† revealing the significant advantage of the Q[8]/Pt NSs in the heterogeneous photocatalysis. It is worth noting that no CO_2 was detected when N_2 instead of CO was used as the starting material, Fig. S37,† unveiling the origin of CO_2 from the CO molecules in the photosynthesis system of the Q[8]/Pt NS films. Besides, the Q[8] support itself was essentially inactive for the photocatalytic CO oxidation reaction under the same reaction conditions, disclosing the essential role of the Pt nanocrystals immobilized at the surface of Q[8] nanosheets in the high activity of the Q[8]/Pt NS films. In addition, the performance of the Q[8]/Pt NS film-20 shows only a negligible drop after five consecutive runs with each run lasting for 40 min under light irradiation, indicating the excellent photostability of the Q[8]/Pt NS films, Fig. 4f and Table S1.† This is further supported by the unchanged morphology, XPS spectrum, and XRD pattern of Q[8]/Pt NS film-20 after the stability tests, Fig. S38–S41.†

Towards further extending the application potential of the present Q[8]/Pt NSs, the continuous thermocatalytic CO oxidation performance of the Q[8]/Pt NS films was also evaluated by a dynamic test with the feed gas (0.8% CO, 20% O_2, and He balance) passing through the Q[8]/Pt NS films in a fixed-bed reactor at a flow rate of 25 mL min^{-1}. As displayed in Fig. 4g, the Q[8]/Pt NS film-10/20/30/40 can achieve the CO oxidation at 40 °C with a specific reaction rate of 396, 540, 576, and 504 $mmol_{CO}\ g_{Pt}^{-1}\ h^{-1}$, respectively, and a CO_2 selectivity of 100%. Along with the increase in temperature, the CO conversion rate increases. At the typical working temperature for polymer electrolyte membrane fuel cells of 80 °C, the CO-to-CO_2 conversion rate of the Q[8]/Pt NS film-10/20/30/40 reaches 9026, 9284, 9437, and 9330 $mmol_{CO}\ g_{Pt}^{-1}\ h^{-1}$, respectively, corresponding to a TOF of 1760, 1810, 1840, and 1819 h^{-1}, Fig. 4h and S42.† In good contrast, no CO_2 was detected for the CH_3OH-reduced Q[8]/Pt film-40 under the same conditions, Fig. S43.† In particular, the catalytic efficiency of the Q[8]/Pt NS films for CO

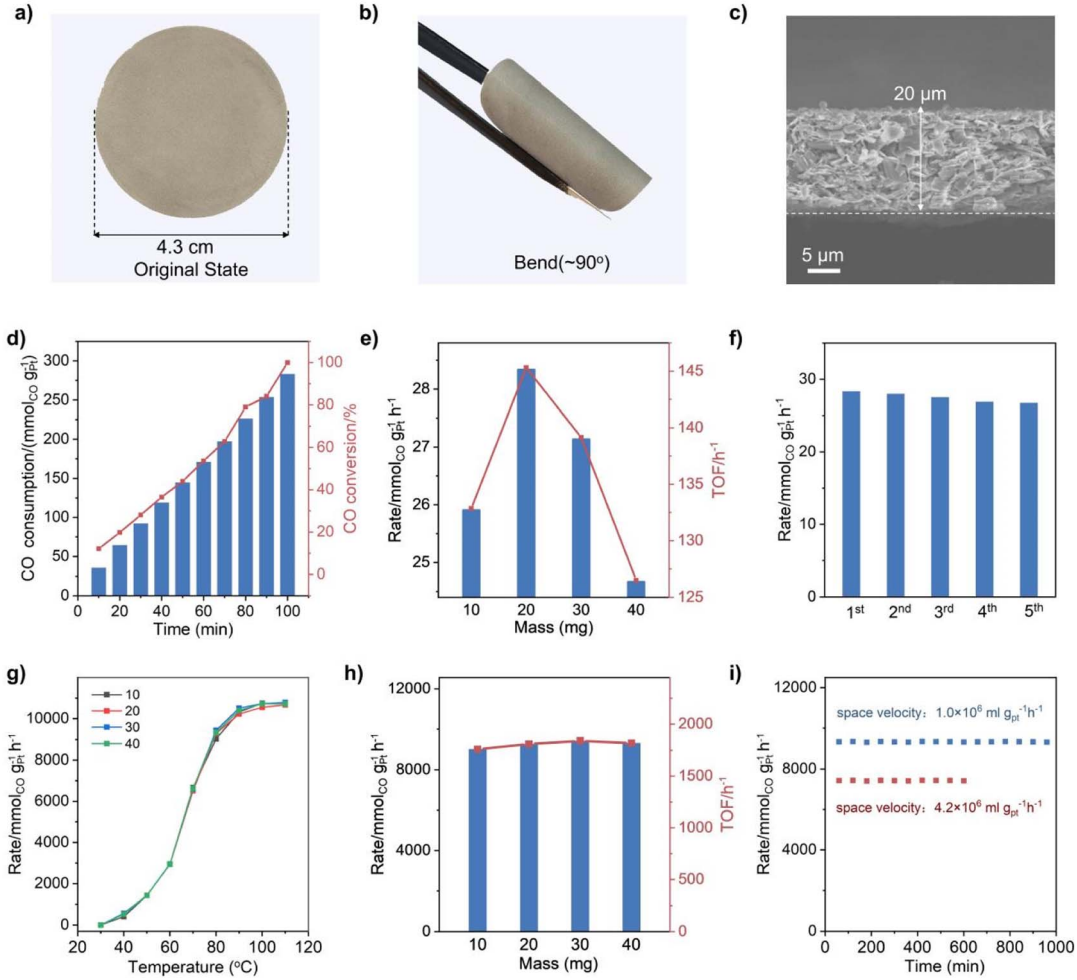

Fig. 4 Photocatalytic and continuous thermocatalytic CO oxidation studies. (a and b) Optical images of the Q[8]/Pt NS film with a thickness of 20 μm as a typical representative. (c) Cross-sectional SEM images of Q[8]/Pt NS film-20. (d) Photocatalytic CO oxidation activities of Q[8]/Pt NS film-20 at 25 °C in an idealized gas mixture (0.8% CO, 20% O_2, He balance). (e) Mass dependence of the reaction rates and TOFs for photocatalytic CO oxidation by Q[8]/Pt NS films. (f) Durability tests of Q[8]/Pt NS film-20 for photocatalysis. (g) Thermocatalytic CO oxidation activities of Q[8]/Pt NS film-10/20/30/40 at 30–80 °C in an idealized gas mixture (0.8% CO, 20% O_2, and He balance). (h) Mass dependence of the reaction rates and TOFs for thermocatalytic CO oxidation by Q[8]/Pt NS films at 80 °C. (i) Durability tests of Q[8]/Pt NS film-40 at 80 °C for thermocatalysis.

oxidation is 1–2 orders of magnitude higher than that of the thus-far reported best supported Pt catalysts and is also much superior to the standard gold nanocatalyst Au/Fe_2O_3, Table S2,† indicating the outstanding performance of the Q[8]/Pt NS films for continuous CO oxidation. Moreover, the CO conversion and the CO_2 selectivity over the Q[8]/Pt NS film-40 remain at constant values over a 1000 minute run under a space velocity of 1.0×10^6 mL g_{Pt}^{-1} h^{-1} at 80 °C, Fig. 4i. Further studies reveal that Q[8]/Pt NS film-40 remains stable for 300 minutes even at a 5 times higher space velocity of 4.2×10^7 mL g_{Pt}^{-1} h^{-1}. Nevertheless, no obvious change could be observed from the TEM, SEM, XRD, and XPS data of the Q[8]/Pt NS films after the stability tests, Fig. S44–S47,† demonstrating the excellent durability of the Q[8]/Pt NS films, compared to the reported state-of-the-art Pt nano-material-based catalysts, Table S2.†

To get an insight into the catalysis mechanism, the adsorption behavior of CO on the catalyst surface was investigated by

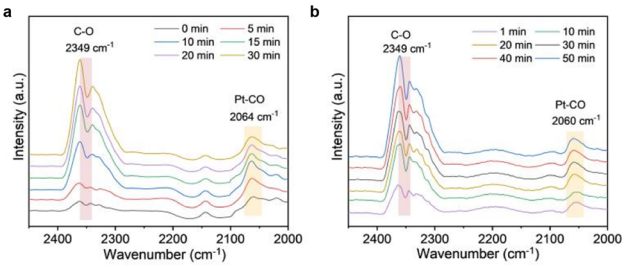

Fig. 5 *In situ* DRIFTS spectroscopic investigation for the CO oxidation performance of the Q[8]/Pt NS films. (a) The light-driven *in situ* DRIFTS spectra of CO adsorption for Q[8]/Pt NS film under visible light irradiation (λ > 400 nm). (b) The thermo-driven *in situ* DRIFTS spectra of CO adsorption for Q[8]/Pt NS film. All DRIFTS measurements were obtained after CO adsorption under 0.8% CO, 20% O_2, and He balance with a flow rate of 100 mL min^{-1}.

in situ DRIFTS spectroscopy. Fig. 5a and b show the visible light-driven and thermo-driven *in situ* DRIFTS spectra, respectively, of Q[8]/Pt NS films under an atmosphere of 0.8% CO, 20% O_2, and remaining He as a function of time. At the beginning of the visible light-driven reaction, the band due to the Pt–CO bond appeared at 2064 cm^{-1}, Fig. 5a, indicating the strong CO adsorption of the Pt nanocrystals.[56,57] In addition, the band due to the C–O stretching vibration of CO_2 at 2349 cm^{-1} gradually increases, revealing the CO-to-CO_2 conversion under the catalysis of Q[8]/Pt NSs.[58,59] This is also true for the thermo-driven reaction, Fig. 5b and S48a,† in line with the DFT calculation results. To further clarify the CO → CO_2 reaction mechanism, DFT calculation was carried out using the optimized Q[8]/Pt NS model, in which Pt nanoparticles are located in the shallow pits at the surface of Q[8] NSs and constructed by three Q[8] molecules, Fig. S48a.† According to the calculation results from this model, when one O_2 molecule is absorbed onto two adjacent Pt atoms, the O–O bond is activated along with the formation of a transition state [*O···O···*C═O] with the potential barrier of 1.17 eV, Fig. S48b,† which could be easily driven by the visible light irradiation or thermal vibration at *ca.* 80 °C. This transition state then gets split into O* and CO_2 with a significant Gibbs free energy decrease as high as 2.49 eV. Along with the leaving of this newly generated CO_2, another CO molecule is attracted onto the same Pt catalytic site and oxidized to CO_2 by the O* with an energy decrease of 1.02 eV, finally completing one catalytic cycle.

Conclusions

In summary, crystalline ultrathin nanosheets of the 3D Q[8] SMF immobilized with Pt nanocrystals on the surface have been fabricated from a solid–liquid chemical reaction under the help of a large amount of gas and heat yielded. This composite with ultrahigh chemical stability exhibits excellent photo-/thermo-catalytic CO oxidation performance with high CO-to-CO_2 conversion efficiency and good durability due to the synergistic effect between Pt nanocrystals and Q[8] molecules in the nanosheets. Crystalline ultrathin nanosheets of 3D SMFs represent a new family of organic molecule-based materials with exceptional structural features and properties for diverse application potentials. This work will hopefully inspire further efforts towards designing and preparing crystalline ultrathin nanosheets of 3D molecule-based frameworks for enhanced functionalities.

Data availability

All the data supporting this article have been included in the main text and the ESI.†

Author contributions

J. Jiang, K. Wang, D. Qi, T. Wang and X. Wang conceived and supervised the project, X. Wang performed the experiments, D. Qi and Y. Jin performed the DFT calculation, T. Zheng performed the X-ray absorption structural data analysis, D. Qi and Ning Li worked on part of the diagrams and models and participated in the discussion of the experimental results. Y. Han performed the SEM experimental characterization, B. Yu performed the single crystal test and analysis, J. Jiang, K. Wang, D. Qi, T. Wang and X. Wang linked the experiments, analysis and calculations, and all the authors discussed and wrote the manuscript.

Conflicts of interest

There is no conflict of interest to report.

Acknowledgements

Financial support from the Natural Science Foundation of China (No. 22235001 and 22175020) and the University of Science and Technology Beijing is gratefully acknowledged. The authors wish to thank the facility support of the 1W2A beamline of the Beijing Synchrotron Radiation Facility (BSRF).

References

1 J. Dong, L. Liu, C. Tan, Q. Xu, J. Zhang, Z. Qiao, D. Chu, Y. Liu, Q. Zhang, J. Jiang, Y. Han, A. P. Davis and Y. Cui, Free-standing homochiral 2D monolayers by exfoliation of molecular crystals, *Nature*, 2022, **602**, 606–611.

2 M. Pfeffermann, R. Dong, R. Graf, W. Zajaczkowski, T. Gorelik, W. Pisula, A. Narita, K. Müllen and X. Feng, Free-Standing Monolayer Two-Dimensional Supramolecular Organic Framework with Good Internal Order, *J. Am. Chem. Soc.*, 2015, **137**, 14525–14532.

3 B. E. R. Snyder, A. B. Turkiewicz, H. Furukawa, M. V. Paley, E. O. Velasquez, M. N. Dods and J. R. Long, A ligand insertion mechanism for cooperative NH_3 capture in metal-organic frameworks, *Nature*, 2023, **613**, 287–291.

4 L.-H. Xu, S.-H. Li, H. Mao, Y. Li, A.-S. Zhang, S. Wang, W.-M. Liu, J. Lv, T. Wang, W.-W. Cai, L. Sang, W.-W. Xie, C. Pei, Z.-Z. Li, Y.-N. Feng and Z.-P. Zhao, Highly flexible and superhydrophobic MOF nanosheet membrane for ultrafast alcohol-water separation, *Science*, 2022, **378**, 308–313.

5 T. Ma, E. A. Kapustin, S. X. Yin, L. Liang, Z. Zhou, J. Niu, L.-H. Li, Y. Wang, J. Su, J. Li, X. Wang, W. D. Wang, W. Wang, J. Sun and O. M. Yaghi, Single-crystal x-ray diffraction structures of covalent organic frameworks, *Science*, 2018, **361**, 48–52.

6 C. Kang, Z. Zhang, S. Kusaka, K. Negita, A. K. Usadi, D. C. Calabro, L. S. Baugh, Y. Wang, X. Zou, Z. Huang, R. Matsuda and D. Zhao, Covalent organic framework atropisomers with multiple gas-triggered structural flexibilities, *Nat. Mater.*, 2023, **22**, 636–643.

7 B. Yu, R.-B. Lin, G. Xu, Z.-H. Fu, H. Wu, W. Zhou, S. Lu, Q.-W. Li, Y. Jin, J.-H. Li, Z. Zhang, H. Wang, Z. Yan, X. Liu, K. Wang, B. Chen and J. Jiang, Linkage conversions in single-crystalline covalent organic frameworks, *Nat. Chem.*, 2023, **16**, 114–124.

8 X. Yang, L. Gong, X. Liu, P. Zhang, B. Li, D. Qi, K. Wang, F. He and J. Jiang, Mesoporous Polyimide-Linked Covalent Organic Framework with Multiple Redox-Active Sites for High-Performance Cathodic Li Storage, *Angew. Chem., Int. Ed.*, 2022, **61**, e202207043.

9 D. Gupta, G. Chanteux, G. Kumar, K. Robeyns and A. Vlad, Modular metallotecton for engineering permanently porous frameworks: supernumerary role of ancillary ion, *Chem. Sci.*, 2023, **14**, 9780–9786.

10 Y. Zhang, L. Yang, L. Wang, X. Cui and H. Xing, Pillar iodination in functional boron cage hybrid supramolecular frameworks for high performance separation of light hydrocarbons, *J. Mater. Chem. A*, 2019, **7**, 27560–27566.

11 G. Zhang, B. Li, Y. Zhou, X. Chen, B. Li, Z.-Y. Lu and L. Wu, Processing supramolecular framework for free interconvertible liquid separation, *Nat. Commun.*, 2020, **11**, 425.

12 G. Zhang, X. Li, G. Chen, Y. Zhang, M. Wei, X. Chen, B. Li, Y. Wu and L. Wu, Supramolecular framework membrane for precise sieving of small molecules, nanoparticles and proteins, *Nat. Commun.*, 2023, **14**, 975.

13 S. Laha, R. Haldar, N. Dwarkanath, S. Bonakala, A. Sharma, A. Hazra, S. Balasubramanian and T. K. Maji, A Dynamic Chemical Clip in Supramolecular Framework for Sorting Alkylaromatic Isomers using Thermodynamic and Kinetic Preferences, *Angew. Chem., Int. Ed.*, 2021, **60**, 19921–19927.

14 Y. Zhang, G. Zhang, B. Li and L. Wu, Non-Stop Switching Separation of Superfine Solid/Liquid Dispersed Phases in Oil and Water Systems Using Polymer-Assisted Framework Fiber Membranes, *Small Methods*, 2023, **7**, 2201455.

15 H. Li, C. Chen, Q. Li, X. J. Kong, Y. Liu, Z. Ji, S. Zou, M. Hong and M. Wu, An Ultra-stable Supramolecular Framework Based on Consecutive Side-by-side Hydrogen Bonds for One-step C_2H_4/C_2H_6 Separation, *Angew. Chem., Int. Ed.*, 2024, e202401754.

16 A. Ozden, J. Li, S. Kandambeth, X.-Y. Li, S. Liu, O. Shekhah, P. Ou, Y. Zou Finfrock, Y.-K. Wang, T. Alkayyali, F. Pelayo García de Arquer, V. S. Kale, P. M. Bhatt, A. H. Ip, M. Eddaoudi, E. H. Sargent and D. Sinton, Energy- and carbon-efficient CO_2/CO electrolysis to multicarbon products *via* asymmetric ion migration–adsorption, *Nat. Energy*, 2023, **8**, 179–190.

17 X. Chen, H. Wu, X. Shi and L. Wu, Polyoxometalate-based frameworks for photocatalysis and photothermal catalysis, *Nanoscale*, 2023, **15**, 9242–9255.

18 X. Liu, J. Zhang, Y. Lan, Q. Zheng and W. Xuan, Infinite building blocks for directed self-assembly of a supramolecular polyoxometalate–cyclodextrin framework for multifunctional oxidative catalysis, *Inorg. Chem. Front.*, 2022, **9**, 6534–6543.

19 X. Lu, Y. Tang, G. Yang and Y.-Y. Wang, Multifunctional lanthanide MOFs with active sites as new platforms for smart sensing of methylmalonic acid and anti-counterfeiting applications, *J. Mater. Chem. C*, 2023, **11**, 2328–2335.

20 S. Mondal, N. Alam, S. Sahoo and D. Sarma, A "heat set" Zr-Diimide based Fibrous Metallogel: Multiresponsive Sensor, Column-based Dye Separation, and Iodine Sequestration, *J. Colloid Interface Sci.*, 2023, **633**, 441–452.

21 Q. Liu, J. Lu, H. Lin, X. Wang, Z. Chang, Y. Chen and Y. Zhang, Polyoxometalate-based metal–organic complexes constructed from a new bis-pyrimidine-amide ligand with high capacitance performance and selectivity for the detection of Cr(VI), *Chin. Chem. Lett.*, 2022, **33**, 4389–4394.

22 B. Li, Q.-Q. Yan and G.-P. Yong, A new porous coordination polymer reveals selective sensing of Fe^{3+}, $Cr_2O_7^{2-}$, CrO_4^{2-}, MnO_4^- and nitrobenzene, and stimuli-responsive luminescence color conversions, *J. Mater. Chem. C*, 2020, **8**, 11786–11795.

23 W. Jia, S. Ren, H. Xia, C. Zhang and J. Zhang, An ultra-stable Cd coordination polymer based on double-chelated ligand for efficient dual-response of TNP and MnO_4, *Sens. Actuators, B*, 2020, **317**, 128230.

24 T. R. Simmons, G. Berggren, M. Bacchi, M. Fontecave and V. Artero, Mimicking hydrogenases: from biomimetics to artificial enzymes, *Coord. Chem. Rev.*, 2014, **270–271**, 127–150.

25 S. Li, B. Wang, G. Liu, X. Li, C. Sun, Z. Zhang and X. Wang, Achieving ultra-trace analysis and multi-light driven photodegradation toward phenolic derivatives *via* a bifunctional catalyst derived from a Cu(I)-complex-modified polyoxometalate, *Inorg. Chem. Front.*, 2024, **11**, 1561–1572.

26 Z. A. Siddiqi, M. Shahid, M. Khalid and S. Kumar, Antimicrobial and SOD activities of novel transition metal ternary complexes of iminodiacetic acid containing α-diimine as auxiliary ligand, *Eur. J. Med. Chem.*, 2009, **44**, 2517–2522.

27 X. Yu, S. U. Khan, Z. Jin, Q. Wu, H. Pang, H. Ma, X. Wang, L. Tan and G. Yang, Water cluster encapsulated polyoxometalate-based hydrogen-bonded supramolecular frameworks (PHSFs) as a new family of high-capacity electrode materials, *J. Energy Storage*, 2022, **53**, 105192.

28 Z.-Q. Shi, N.-N. Ji, K.-M. Guo and G. Li, Crystalline hydrogen-bonded supramolecular frameworks (HSFs) as new class of proton conductive materials, *Appl. Surf. Sci.*, 2020, **504**, 144484.

29 K. S. Novoselov, A. K. Geim, S. V. Morozov, D. Jiang, Y. Zhang, S. V. Dubonos, I. V. Grigorieva and A. A. Firsov, Electric Field Effect in Atomically Thin Carbon Films, *Science*, 2004, **306**, 666–669.

30 L. P. Skala, C. L. Stern, L. Bancroft, C. M. Moisanu, C. Pelkowski, X. Aguilar-Enriquez, J. L. Swartz, M. R. Wasielewski and W. R. Dichtel, A modular platform for the precise assembly of molecular frameworks composed of ion pairs, *Chem*, 2023, **9**, 1208–1220.

31 B. Baris, V. Luzet, E. Duverger, P. Sonnet, F. Palmino and F. Cherioux, Robust and Open Tailored Supramolecular Networks Controlled by the Template Effect of a Silicon Surface, *Angew. Chem., Int. Ed.*, 2011, **50**, 4094–4098.

32 M. Zhao, Y. Huang, Y. Peng, Z. Huang, Q. Ma and H. Zhang, Two-dimensional metal-organic framework nanosheets: synthesis and applications, *Chem. Soc. Rev.*, 2018, **47**, 6267–6295.

33 Y. Peng, Y. Li, Y. Ban, H. Jin, W. Jiao, X. Liu and W. Yang, Metal-organic framework nanosheets as building blocks for molecular sieving membranes, *Science*, 2014, **346**, 1356–1359.

34 D. Rodríguez-San-Miguel, C. Montoro and F. Zamora, Covalent organic framework nanosheets: preparation, properties and applications, *Chem. Soc. Rev.*, 2020, **49**, 2291–2302.

35 J. W. Colson, A. R. Woll, A. Mukherjee, M. P. Levendorf, E. L. Spitler, V. B. Shields, M. G. Spencer, J. Park and W. R. Dichtel, Oriented 2D Covalent Organic Framework Thin Films on Single-Layer Graphene, *Science*, 2011, **332**, 228–231.

36 W. Liu, X. Li, C. Wang, H. Pan, W. Liu, K. Wang, Q. Zeng, R. Wang and J. Jiang, A Scalable General Synthetic Approach toward Ultrathin Imine-Linked Two-Dimensional Covalent Organic Framework Nanosheets for Photocatalytic CO_2 Reduction, *J. Am. Chem. Soc.*, 2019, **141**, 17431–17440.

37 J. Li, X. Jing, Q. Li, S. Li, X. Gao, X. Feng and B. Wang, Bulk COFs and COF nanosheets for electrochemical energy storage and conversion, *Chem. Soc. Rev.*, 2020, **49**, 3565–3604.

38 X. Li, H.-S. Xu, K. Leng, S. W. Chee, X. Zhao, N. Jain, H. Xu, J. Qiao, Q. Gao, I.-H. Park, S. Y. Quek, U. Mirsaidov and K. P. Loh, Partitioning the interlayer space of covalent organic frameworks by embedding pseudorotaxanes in their backbones, *Nat. Chem.*, 2020, **12**, 1115–1122.

39 J. Yang, B. Tu, G. Zhang, P. Liu, K. Hu, J. Wang, Z. Yan, Z. Huang, M. Fang, J. Hou, Q. Fang, X. Qiu, L. Li and Z. Tang, Advancing osmotic power generation by covalent organic framework monolayer, *Nat. Nanotechnology*, 2022, **17**, 622–628.

40 S. Zhao, Y. Wang, J. Dong, C.-T. He, H. Yin, P. An, K. Zhao, X. Zhang, C. Gao, L. Zhang, J. Lv, J. Wang, J. Zhang, A. M. Khattak, N. A. Khan, Z. Wei, J. Zhang, S. Liu, H. Zhao and Z. Tang, Ultrathin metal-organic framework nanosheets for electrocatalytic oxygen evolution, *Nat. Energy*, 2016, **1**, 16184.

41 A. Pustovarenko, M. G. Goesten, S. Sachdeva, M. Shan, Z. Amghouz, Y. Belmabkhout, A. Dikhtiarenko, T. Rodenas, D. Keskin, I. K. Voets, B. M. Weckhuysen, M. Eddaoudi, L. C. P. M. de Smet, E. J. R. Sudhölter, F. Kapteijn, B. Seoane and J. Gascon, Nanosheets of Nonlayered Aluminum Metal-Organic Frameworks through a Surfactant-Assisted Method, *Adv. Mater.*, 2018, **30**, 1707234.

42 S. J. Datta, A. Mayoral, N. Murthy Srivatsa Bettahalli, P. M. Bhatt, M. Karunakaran, I. D. Carja, D. Fan, P. G. M. Mileo, R. Semino, G. Maurin, O. Terasaki and M. Eddaoudi, Rational design of mixed-matrix metal-organic framework membranes for molecular separations, *Science*, 2022, **376**, 1080–1087.

43 P. Falcaro, A. J. Hill, K. M. Nairn, J. Jasieniak, J. I. Mardel, T. J. Bastow, S. C. Mayo, M. Gimona, D. Gomez, H. J. Whitfield, R. Riccò, A. Patelli, B. Marmiroli, H. Amenitsch, T. Colson, L. Villanova and D. Buso, A new method to position and functionalize metal-organic framework crystals, *Nat. Commun.*, 2011, **2**, 237.

44 S. Chen, C. Zhu, W. Xian, X. Liu, X. Liu, Q. Zhang, S. Ma and Q. Sun, Imparting Ion Selectivity to Covalent Organic Framework Membranes Using *de Novo* Assembly for Blue Energy Harvesting, *J. Am. Chem. Soc.*, 2021, **143**, 9415–9422.

45 Y. Yang, M. Ratsch, A. M. Evans and K. Börjesson, Layered 3D Covalent Organic Framework Films Based on Carbon-Carbon Bonds, *J. Am. Chem. Soc.*, 2023, **145**, 18668–18675.

46 T. Zhu, Y. Kong, B. Lyu, L. Cao, B. Shi, X. Wang, X. Pang, C. Fan, C. Yang, H. Wu and Z. Jiang, 3D covalent organic framework membrane with fast and selective ion transport, *Nat. Commun.*, 2023, **14**, 5926.

47 X. Shi, Z. Zhang, C. Yin, X. Zhang, J. Long, Z. Zhang and Y. Wang, Design of Three-Dimensional Covalent Organic Framework Membranes for Fast and Robust Organic Solvent Nanofiltration, *Angew. Chem., Int. Ed.*, 2022, **61**, e202207559.

48 G. Yun, Z. Hassan, J. Lee, J. Kim, N.-S. Lee, N. H. Kim, K. Baek, I. Hwang, C. G. Park and K. Kim, Highly Stable, Water-Dispersible Metal-Nanoparticle-Decorated Polymer Nanocapsules and Their Catalytic Applications, *Angew. Chem., Int. Ed.*, 2014, **53**, 6414–6418.

49 P. Wang, X. Zhang, J. Zhang, S. Wan, S. Guo, G. Lu, J. Yao and X. Huang, Precise tuning in platinum-nickel/nickel sulfide interface nanowires for synergistic hydrogen evolution catalysis, *Nat. Commun.*, 2017, **8**, 14580.

50 C. Guo, Y. Jiao, Y. Zheng, J. Luo, K. Davey and S.-Z. Qiao, Intermediate Modulation on Noble Metal Hybridized to 2D Metal-Organic Framework for Accelerated Water Electrocatalysis, *Chem*, 2019, **5**, 2429–2441.

51 M. Wang, Y. Xu, C.-K. Peng, S.-Y. Chen, Y.-G. Lin, Z. Hu, L. Sun, S. Ding, C.-W. Pao, Q. Shao and X. Huang, Site-Specified Two-Dimensional Heterojunction of Pt Nanoparticles/Metal-Organic Frameworks for Enhanced Hydrogen Evolution, *J. Am. Chem. Soc.*, 2021, **143**, 16512–16518.

52 H. You, D. Wu, Z.-n. Chen, F. Sun, H. Zhang, Z. Chen, M. Cao, W. Zhuang and R. Cao, Highly Active and Stable Water Splitting in Acidic Media Using a Bifunctional Iridium/Cucurbit[6]uril Catalyst, *ACS Energy Lett.*, 2019, **4**, 1301–1307.

53 T. Ma, H. Cao, S. Li, S. Cao, Z. Zhao, Z. Wu, R. Yan, C. Yang, Y. Wang, P. A. van Aken, L. Qiu, Y.-G. Wang and C. Cheng, Crystalline Lattice-Confined Atomic Pt in Metal Carbides to Match Electronic Structures and Hydrogen Evolution Behaviors of Platinum, *Adv. Mater.*, 2022, **34**, 2206368.

54 X. Shi, C. Dai, X. Wang, J. Hu, J. Zhang, L. Zheng, L. Mao, H. Zheng and M. Zhu, Protruding Pt single-sites on hexagonal $ZnIn_2S_4$ to accelerate photocatalytic hydrogen evolution, *Nat. Commun.*, 2022, **13**, 1287.

55 J. Wei, K. Xiao, Y. Chen, X.-P. Guo, B. Huang and Z.-Q. Liu, *In situ* precise anchoring of Pt single atoms in spinel Mn_3O_4 for a highly efficient hydrogen evolution reaction, *Energy Environ. Sci.*, 2022, **15**, 4592–4600.

56 X. Li, X. I. Pereira-Hernández, Y. Chen, J. Xu, J. Zhao, C.-W. Pao, C.-Y. Fang, J. Zeng, Y. Wang, B. C. Gates and

J. Liu, Functional CeOx nanoglues for robust atomically dispersed catalysts, *Nature*, 2022, **611**, 284–288.

57 B. Qiao, A. Wang, X. Yang, L. F. Allard, Z. Jiang, Y. Cui, J. Liu, J. Li and T. Zhang, Single-atom catalysis of CO oxidation using Pt1/FeOx, *Nat. Chem.*, 2011, **3**, 634–641.

58 A. M. Abdel-Mageed, B. Rungtaweevoranit, S. Impeng, J. Bansmann, J. Rabeah, S. Chen, T. Häring, S. Namuangrak, K. Faungnawakij, A. Brückner and R. J. Behm, Unveiling the CO Oxidation Mechanism over a Molecularly Defined Copper Single-Atom Catalyst Supported on a Metal–Organic Framework, *Angew. Chem., Int. Ed.*, 2023, e202301920.

59 V. Muravev, A. Parastaev, Y. van den Bosch, B. Ligt, N. Claes, S. Bals, N. Kosinov and E. J. M. Hensen, Size of cerium dioxide support nanocrystals dictates reactivity of highly dispersed palladium catalysts, *Science*, 2023, **380**, 1174–1179.